



Influence of copper on nickel-based catalysts in the conversion of glycerol



B.C. Miranda^{a,b}, R.J. Chimentão^{a,f,*}, J. Szanyi^c, A.H. Braga^d, J.B.O. Santos^d,
F. Gispert-Guirado^a, J. Llorca^e, F. Medina^a

^a Universitat Rovira i Virgili, Tarragona 43007, Spain

^b Universidad de Costa Rica, San José 2060, Costa Rica

^c Institute for Integrated Catalysis, Pacific Northwest National Laboratory, PO Box 999, MS K8-86, Richland, WA 99352, USA

^d Departamento de Engenharia Química, Universidade Federal de São Carlos, São Carlos, Brazil

^e Institut de Tècniques Energètiques, Universitat Politècnica de Catalunya, Barcelona, Spain

^f School of Chemistry, Yachay Tech, Yachay City of Knowledge, Urcuquí, Ecuador

ARTICLE INFO

Article history:

Received 9 September 2014

Received in revised form 27 October 2014

Accepted 8 November 2014

Available online 18 November 2014

Keywords:

Hydrogenolysis

Dehydration

Glycerol

Nickel

Copper

ABSTRACT

The catalytic transformation of glycerol to value-added compounds was investigated over bimetallic Ni–Cu/ γ -Al₂O₃ catalysts with Ni/Cu atomic ratios of 8/1, 4/1, 2/1, 1/1, 1/2, 1/4, and 1/8. XPS analysis revealed that the surface composition of the catalyst exhibited progressive enrichment of Cu as its content in the catalyst increased. H₂-chemisorption indicated that the total number of exposed Ni atoms decreased as the Cu content increased. As a result, deep hydrogenolysis to produce CH₄ was inhibited by the addition of Cu to the Ni catalyst, yielding higher selectivity toward the dehydration products of glycerol such as hydroxyacetone.

FTIR spectra of adsorbed CO reveal that Cu asserts both geometric and electronic effects on the adsorption properties of Ni. The geometrical effect is visualized by the progressive disappearance of the bridge-bound adsorbed CO on metallic Ni by the incorporation of Cu. This suggests that the deep hydrogenolysis of glycerol to CH₄ formation requires an ensemble of adjacent active Ni atoms. The electronic effect of Cu on Ni is indicated by the red shift of the IR peak of adsorbed CO as the Cu content increases. The electronic interaction between Cu and Ni species was also substantiated by XANES results. HTREM revealed metal particles very well distributed on the support with particle size of 1.5 to 5 nm. The Ni–Cu samples were not a total intermetallic alloys.

© 2014 Elsevier B.V. All rights reserved.

1. Introduction

Glycerol has been produced as a byproduct from saponification and hydrolysis reactions. Nowadays glycerol is also available as an inevitable by-product in biodiesel production generating approximately 10% of crude glycerol by volume [1]. Since biodiesel production worldwide is increasing, the availability of glycerol will also increase. In this respect, new applications for glycerol need to be developed [2,3] to overcome its excess. Efficient processes for glycerol transformation into valuable chemicals, such as hydrogenolysis, dehydrogenation, and dehydration are highly desirable [4,5].

The hydrogenolysis of glycerol is supposed to occur through two mechanisms: (i) the route of hydroxyacetone and (ii) the route of

glyceraldehyde. The route of hydroxyacetone [6] involves the glycerol dehydration to form hydroxyacetone which is sequentially hydrogenated to 1,2-propanediol (1,2-PDO). The most plausible mechanism reaction for the glyceraldehyde route was proposed by Montassier et al. [7] which involves a dehydrogenation of glycerol to glyceraldehyde followed by hydrogenation to form ethylene glycol (EG) and methanol. Finally, methane (CH₄) is formed by deep hydrogenolysis. The dehydration of glycerol to hydroxyacetone is catalyzed by acid sites and this reaction occurs via protonation of the terminal hydroxyl group with consecutive elimination of water molecule and formation of an enol intermediate [8,9].

The use of noble metal catalysts containing Ru [10,11], Pt [12–14], Rh [15–18], Pd [15,16,19], and Ir [20] have been reported in the hydrogenolysis of glycerol. Metallic systems based on noble metals can be a drawback to development of the hydrogenolysis process. The use of non-noble bimetallic catalysts has been proposed for hydrogenation and hydrogenolysis reactions. Replacement of noble metal catalysts with cheap and abundant

* Corresponding author. Tel.: +(593) 23949100x2004.

E-mail address: rchimenton@yachaytech.edu.ec (R.J. Chimentão).

metals is a major goal for a sustainable chemistry. Nickel (Ni) and copper (Cu) are cheap metals and, therefore, are ideal candidates. Jiménez-Morales et al. [21] reported that the hydrogenolysis of glycerol at 473 K and 2.4 MPa of H_2 on Ni supported on SBA-15 led to volatile products by C–C hydrogenolysis. Unlike Ni, Cu is effective at breaking C–O bonds and avoids C–C bonds cleavages [9]. Copper catalysts have been used to produce 1,2-PDO with high yield. Sato et al. [9] observed that the addition of acidic oxide support such as Al_2O_3 , ZrO_2 , Fe_2O_3 and SiO_2 to Cu enhanced the selectivity to hydroxyacetone.

Recently, we have studied the conversion of glycerol in gas phase at 573 K and atmospheric pressure over Ni based catalyst [22]. We proposed a general reaction pathway for glycerol conversion. Several routes of glycerol transformation such as dehydration, dehydrogenation and hydrogenolysis were observed producing mainly hydroxyacetone, pyruvaldehyde, pyruvic acid, methyl lactate, lactide, acetaldehyde and CH_4 . Undesired side reactions such as coke formation were observed on 10% Ni/ γ - Al_2O_3 catalysts. Coke was the major cause of catalyst deactivation in the glycerol conversion. The use of a bimetallic catalyst can be an alternative to minimize the catalyst deactivation. The introduction of a second metal to the Ni catalyst may provide significant changes in the catalytic activity and selectivity as compared with the monometallic one, as observed in other works [23,24].

Understanding the mechanism of the cleavage of the C–C and C–O bonds which modulates the routes in the glycerol conversion (dehydration, dehydrogenation, and hydrogenolysis) is the key to control the selectivity to valuable products such as hydroxyacetone and lactic acid. A good example of the modification of catalytic activity with composition is the use of bimetallic Ni–Cu catalysts [25]. The hydrogenolytic capacity of Cu to the cleavage of C–C bonds is poor. However, Cu is an efficient catalyst for the cleavage of C–O bonds which can dramatically affect the Ni based catalysts in the product distribution of the glycerol conversion. In particular, bimetallic Ni–Cu systems can present advantages with respect to monometallic Ni catalysts. Gandarias et al. [26] used Ni–Cu/ Al_2O_3 in the glycerol hydrogenolysis to 1,2-PDO under N_2 pressure and formic acid as hydrogen donor molecule. These authors observed that the Ni/Cu atomic ratio and acid sites affected the yield to 1,2-PDO. In addition, the reduction of Ni–Cu/ Al_2O_3 led to formation of Ni–Cu alloy inhibiting the activity for C–C bond cleavage. The effect of Cu on Ni in the reaction routes of glycerol (dehydration, dehydrogenation, hydrogenolysis) may be rationalized by the formation of different chemisorbed intermediates on the catalyst surface, resulting in different products [27,28]. The present work is devoted to study the effect of Cu introduction into Ni in the catalytic conversion of glycerol. Catalysts with different Ni/Cu atomic ratios were prepared and tested. The physical and chemical properties of Ni–Cu and monometallic samples were examined by X-ray diffraction (XRD), X-ray absorption near edge structure (XANES), in situ FTIR of adsorbed CO, H_2 -chemisorption, temperature programmed desorption of NH_3 (TPD- NH_3), X-ray photoelectron spectroscopy (XPS), temperature programmed reduction (TPR), high resolution transmission electron microscopy (HRTEM), N_2 -physisorption and temperature programmed oxidation (TPO).

2. Experimental

2.1. Catalyst preparation

Commercial γ - Al_2O_3 was purchased from Degussa. It was calcined at 463 K for 4 h before use. The Ni–Cu catalysts containing 10 wt.% of total metal loading were prepared by wet co-impregnation of γ - Al_2O_3 with an aqueous solution containing the $Ni(NO_3)_2 \cdot 6H_2O$ and $Cu(NO_3)_2 \cdot 6H_2O$ precursors, which were

mixed to obtain the following Ni:Cu atomic ratios: NiCu81, NiCu41, NiCu21, NiCu11, NiCu12, NiCu14 and NiCu18. It was also prepared the monometallic Ni sample and the monometallic Cu sample. After co-impregnation, each sample was dried by rotavapor at 373 K for 12 h and it was then reduced at 723 K in a flow of 20 mL/min with pure H_2 for 4 h.

2.2. Catalyst characterization

2.2.1. Thermal decomposition of $Ni(NO_3)_2 \cdot 6H_2O$ and $Cu(NO_3)_2 \cdot 6H_2O$ co-impregnated over γ - Al_2O_3 under hydrogen flow

The decomposition temperature of $Ni(NO_3)_2 \cdot 6H_2O$ and $Cu(NO_3)_2 \cdot 6H_2O$ precursors was investigated by TGA-MS over all dried co-impregnated samples. TGA were recorded in a Sensys evo apparatus from 323 K to 1023 K, at a heating rate of 10 K/min under a flow of 5% H_2 /Ar. The off-gas was simultaneously analyzed with a Pfeiffer Vacuum QME 220 mass spectrometer (MS).

2.2.2. Temperature programmed reduction (TPR)

TPR experiments were performed in a ThermoFinnigan (TPORD 110) apparatus equipped with a thermal conductivity detector (TCD). The samples were then purged with Ar flow before the TPR analysis. The analysis was carried out using a 5% H_2 /Ar gas flowing at 20 mL/min by heating from room temperature (RT) to 1173 K with a heating rate of 10 K/min. The evolved species during TPR were monitored by an on-line mass spectrometer Pfeiffer Vacuum QME 220. Soda lime was used as trap in order to stop NO_x gases in the carrier gas before they enter the detector.

2.2.3. N_2 -adsorption-desorption

The specific surface area, cumulative pore volume and average pore diameter of the samples were measured by the BET method using N_2 adsorption/desorption at 77 K in a Quantachrome Autosorb-1. Before measurement, each sample was degassed under vacuum at 393 K overnight. The BET specific surface area was calculated from the range $P/P_0 = 0.05$ –0.35 in the adsorption branch while the pore size distribution was calculated from the desorption branch.

2.2.4. Temperature programmed desorption of NH_3 (TPD- NH_3)

The total acidity measurements of the fresh catalysts were determined by TPD of NH_3 on a Micromeritics AutoChem II equipped with a TCD detector. Each sample (50 mg) was pretreated with Ar at 353 K during 1 h in a tubular down flow quartz reactor and then cooled to RT. The sample was then treated with NH_3 flow (5% NH_3 in He) at RT for 1 h. The NH_3 desorption was measured by heating the sample from RT to 973 K at a heating rate of 10 K/min in He flow. The total number of acid sites was calculated by using pulses of a known amount of NH_3 .

2.2.5. X-ray diffraction (XRD)

The XRD analysis of the materials was recorded using a Siemens D5000 diffractometer (Bragg-Brentano for focusing geometry and vertical θ - θ goniometer) with an angular 2θ -diffraction range between 5° and 90° . The samples were dispersed on a Si(5 1 0) sample holder. The data were collected with an angular step of 0.03° at 5 s per step and sample rotation. Cu $K\alpha$ radiation ($\lambda = 1.54056 \text{ \AA}$) was obtained from a copper X-ray tube operated at 40 kV and 30 mA. For some of the samples, the angular 2θ -diffraction range was between 3° and 60° .

2.2.6. High resolution transmission electron microscopy (HRTEM)

HRTEM was carried out with a JEOL J2010F electron microscope equipped with a field emission gun operating at an accelerating voltage of 200 kV. The samples were prepared by dispersing the

as-prepared catalysts in alcohol in an ultrasonic bath and then dropping the supernatant suspension onto a holey carbon coated grid.

2.2.7. H_2 -chemisorption

H_2 -chemisorption was performed to determine the total area of the exposed metallic Ni atoms according previous work [29]. The analysis was performed using a conventional static method in a Micromeritics 2010 instrument. The samples were heated in flowing He at 400 K for 1 h and then the temperature was increased to the correspondent reduction temperature. At this temperature, the He flow was switched for the H_2 flow and the samples were reduced for 2 h and subsequently out-gassed for 30 min. Finally, the samples were cooled to RT and evacuated at RT for 30 min. The hydrogen adsorption isotherm was recorded at RT. After evacuation at RT for 10 min, a second H_2 isotherm was obtained. The chemisorbed H_2 uptake was obtained by extrapolating to zero pressure the linear portion of the isotherm. The number of exposed Ni atoms was calculated assuming spherical particles, the stoichiometry factor of 1 atomic chemisorbed hydrogen per surface Ni atom, a Ni surface area of 0.065 nm^2 per Ni atom and a Ni density of 8.9 g/cm^3 [29].

2.2.8. X-ray photoelectron spectroscopy (XPS)

The XPS spectra were acquired in a VG Escalab 200R electron spectrometer equipped with a hemispherical electron analyzer, operating in a constant pass energy mode, and a non-monochromatic Mg-K α ($h\nu = 1253.6 \text{ eV}$, $1 \text{ eV} = 1.603 \times 10^{-19} \text{ J}$). X-ray source was operated at 10 mA and 1.2 kV. The angle of the incident photon beam was 45° with respect to the normal of the sample. The background pressure in the analysis chamber was kept below $7 \times 10^{-9} \text{ mbar}$ during data acquisition. The binding energy (BE C1s = 284.9 eV) of adventitious C1 was used as reference. A Shirley background subtraction was applied and Gaussian–Lorentzian product functions were used to approximate the line shapes of the fitting components.

2.2.9. FTIR of adsorbed CO

The IR measurements were carried out on a Vertex-70 (Bruker) spectrometer equipped with a MCT detector, operating at 4 cm^{-1} . The in situ infrared cell used was a 2.75 in six-way stainless steel cube equipped with KBr windows. The cell is connected to a gas handling/pumping station and through both leak and gate valves to a quadruple mass spectrometer (UTI 100C). The catalyst was pressed onto a fine tungsten mesh, which, in turn was mounted onto a copper sample holder assembly attached to ceramic feedthroughs of a 1.33 inch flange. The sample temperature was monitored through a chromel/alumel (K-type) thermocouple spot-welded to the top center of the tungsten mesh. The sample could be heated resistively to $\sim 1000 \text{ K}$ and cooled with liquid nitrogen to $\sim 90 \text{ K}$.

Prior to the IR measurements the sample was heated to 773 K and kept at that temperature for about 2 h to ensure the complete removal of water from the catalyst. FTIR spectra of adsorbed CO were acquired from the in situ reduced (at 773 K) samples at $\sim 300 \text{ K}$. All the samples were reduced at 773 K two times: for 30 min and then for 10 min in $\sim 0.5 \text{ Torr}$ of H_2 . The cell was evacuated between the reduction steps and after the second reduction step. The base pressure of the IR cell following the reduction with H_2 was less than $5 \times 10^{-8} \text{ Torr}$. CO adsorption measurements on the reduced samples were carried out at $\sim 300 \text{ K}$. Prior to each spectral series acquisition, a background spectrum was taken of the clean, freshly reduced sample.

For each sample stepwise CO adsorption was performed until the final CO pressure in the cell reached 0.350 Torr for the Ni, 0.2 Torr for the Cu and 0.350 Torr for the Ni/Cu sample. After equilibration the cell was evacuated for 10 min at 300 K (in order

to remove weakly held CO) and the FTIR spectrum of strongly adsorbed CO was recorded. At the conclusion of each spectral acquisition the sample was heated in vacuum: the Ni sample to 650 K (IR at every 50 K at RT), the Cu sample to 400 K, and the Ni/Cu bimetallic sample to 600 K and the desorbing CO was followed by the mass spectrometer.

2.2.10. X-ray absorption near edge structure (XANES)

XANES spectra at the Ni K-edge (8333 eV) and Cu K-edge: (8980 eV) for impregnated samples were measured at the DXAS beamline of the Brazilian Synchrotron Light Laboratory (LNLS, Campinas, Brazil). The impregnated samples were first crushed and sieved to particle sizes smaller than $20 \mu\text{m}$. A self-supported pellet (60.0 mg of catalyst diluted in 60.0 mg of boron nitride) was prepared and placed inside of a tubular quartz reactor (20 mm ID and 440 mm X-ray path length), equipped with kaptonTM refrigerated windows. Then, temperature-resolved XANES spectra were acquired during in situ reduction of the sample using 5% H_2 in He, flowing at 100 mL/min, with heating at a rate of 10 K/min from RT to 973 K. Ni foil and NiO were used as standards samples to measure the valence state of metallic Ni and oxidized Ni, while Cu foil, Cu_2O and CuO were used as standards samples for Cu species.

2.2.11. Temperature programmed oxidation (TPO-MS)

The amount of coke deposited on the spent catalysts was determined by TPO. The oxidation experiments were carried out with a Sensys evo apparatus. TPO profiles were obtained using approximately 12 mg of sample, which one was loaded in quartz reactor (DI = 0.5 cm and length = 10 cm) and it was heated from 373 K to 823 K at a linearly programmed rate of 10 K/min in air flow. The produced CO_2 amount was determined by an on-line mass spectrometer (MS) Pfeiffer Vacuum QME 220.

2.2.12. Raman spectroscopy

Raman spectra of the spent 10% NiCu/ $\gamma\text{-Al}_2\text{O}_3$ catalysts were obtained by using a T64000 Jobin Ivon spectrometer. Approximately 10 mg of each sample was excited using an Ar laser operating at 514.5 nm and a power of 2 mW.

2.3. Conversion of glycerol

The catalytic conversion of glycerol was carried out in gas phase in a quartz fixed bed down flow reactor at 573 K for 6 h. Typically 100 mg of sample in pellets form with particle size ranging 2–3 mm was loaded in the quartz reactor. Details of experiment can be obtained in our previous work [22]. An aqueous solution of glycerol (3 v/v%) was pumped by a syringe pump with flow of 3.5 mL/h and injected into the reactive gas. Previous to entrance to the reactor the reactive mixture in a $H_2/\text{C}_3\text{H}_8\text{O}_3$ molar ratio of 10 was pre-heated at 573 K and the reaction was carried out at 573 K for 6 h. The condensed products were trapped in a condenser with ice bath and analyzed each 20 min of reaction by High Performance Liquid Chromatography (HPLC, Agilent technologies 1100 series) equipped with a ICSEP ICE-COREGEL 87H3 Column serial No. 12525124 column, a diode-array detector (DAD) and a refractive index (RID) detector. The outlet of the reactor was also connected by a six-way valve to a gas chromatograph equipped with a FID detector and a HP Poraplot column (30 m \times 0.53 mm \times 0.6 m) to analyze the gaseous products. Finally, a total organic carbon (TOC) analyzer (Shimadzu TOC-5000A) was used to check the carbon balance. The conversion of the glycerol was defined as follows:

$$\text{conversion of glycerol (\%)} = \frac{\text{moles of glycerol reacted}}{\text{initial moles of glycerol}} \times 100$$

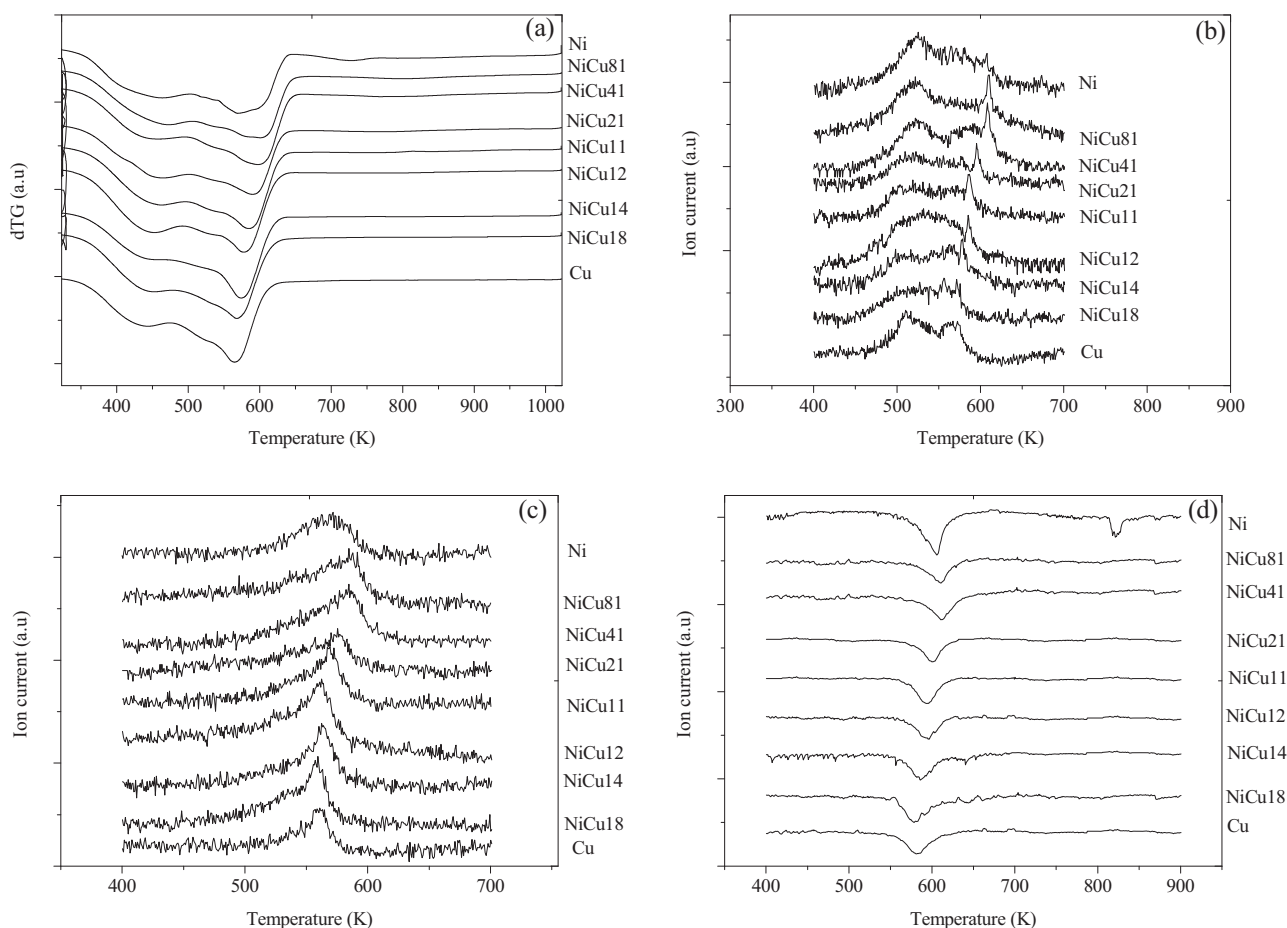


Fig. 1. (a) DTG profiles of the decomposition of metal nitrate precursors, (b) evolution of N_2O ($m/z=44$), (c) evolution of NO_2 ($m/z=46$), and (d) consumption of H_2 ($m/z=2$).

The selectivity to each product was defined as selectivity based on carbon, where:

$$\text{selectivity (\%)} = \frac{\text{moles of carbon in specific product}}{\text{moles of carbon in all products}} \times 100$$

In order to investigate the role of the Cu in the reaction pathway, hydroxyacetone, pyruvaldehyde and lactic acid were used as reactants under the same operation conditions performed for the catalytic conversion of glycerol over the monometallic Cu catalyst.

3. Results

3.1. Catalyst characterization

3.1.1. Thermal decomposition of $\text{Ni}(\text{NO}_3)_2 \cdot 6\text{H}_2\text{O}$ and/or $\text{Cu}(\text{NO}_3)_2 \cdot 6\text{H}_2\text{O}$ impregnated over $\gamma\text{-Al}_2\text{O}_3$ under H_2 flow

All impregnated samples were characterized by TGA-MS and the results are shown in Fig. 1. The decomposition of metal nitrate precursor in monometallic samples occurs below 620 K (Fig. 1a) with an evolution of N_2O ($m/z=44$) (Fig. 1b) and NO_2 ($m/z=46$) (Fig. 1c) species between 450 and 620 K, as well as the consumption of H_2 ($m/z=2$) (Fig. 1d). Fig. 1 reveals that the nitrate species in bimetallic samples are decomposed in a similar way that those showed for monometallic samples and N_2O , NO_2 , and H_2 were observed in all experiments.

Fig. 2 shows the XRD patterns of the impregnated Cu nitrate precursor over $\gamma\text{-Al}_2\text{O}_3$ under in situ reduction with flow of H_2 . The in situ XRD showed that the total decomposition of the Cu nitrate phase occurred around 600 K in agreement with TGA-MS and TPR (vide infra). Two main peaks assigned to $\text{Cu}_2(\text{OH})_3\text{NO}_3$

(Gerhardite, ICDD 14-687) are evident in the diffractogram when the dried impregnated sample was heated from RT to about 550 K, suggesting that the $\text{Cu}(\text{NO}_3)_2 \cdot 6\text{H}_2\text{O}$ was converted to $\text{Cu}_2(\text{OH})_3\text{NO}_3$. Then, $\text{Cu}_2(\text{OH})_3\text{NO}_3$ is decomposed to Cu oxides species around 550 K and the Cu oxides species (Fig. 2) are reduced to metallic Cu at about 600 K. The XRD peaks for metallic Cu are around 600 K, corresponding to the planes (1 1 1) and (2 0 0) (ICDD 4-836). The XRD measurements also revealed reflections corresponding to $\gamma\text{-Al}_2\text{O}_3$ (ICDD 79-1558) and $\alpha\text{-Al}_2\text{O}_3$ (ICDD 46-1212).

3.1.2. TPR

The TPR profiles of the bimetallic Ni–Cu and monometallic Ni and Cu catalysts are shown in Fig. 3. The TPR profile of the monometallic Ni sample displays one peak at 574 K (Fig. 3a), and a broader peak at 749 K (Fig. 3b). The first peak is due to the decomposition of the Ni nitrate precursor to Ni in its oxidized state [30–33] while the second peak is attributed to the reduction of nickel oxide species to metallic Ni [34]. For monometallic Cu sample, the reduction peak between 500 and 550 K (Fig. 3a) can be attributed to two step reduction of CuO to Cu_2O and Cu_2O to metallic Cu [35]. This is consistent with our in situ XRD studies (Fig. 2) of the reduction of the Cu nitrate precursor impregnated on $\gamma\text{-Al}_2\text{O}_3$. The bimetallic catalysts show two reduction zones: the first one between 500 and 620 K (Fig. 3a), and the second one between 600 and 1000 K (Fig. 3b). For samples containing a Ni/Cu atomic ratio less than 1 the first peak is shifted to lower reduction temperatures as the Ni/Cu atomic ratio decreases. For samples containing higher amount of Ni the first peak is quite similar to that of monometallic Ni sample. The second peak between 600 and 1000 K shifts to lower temperatures

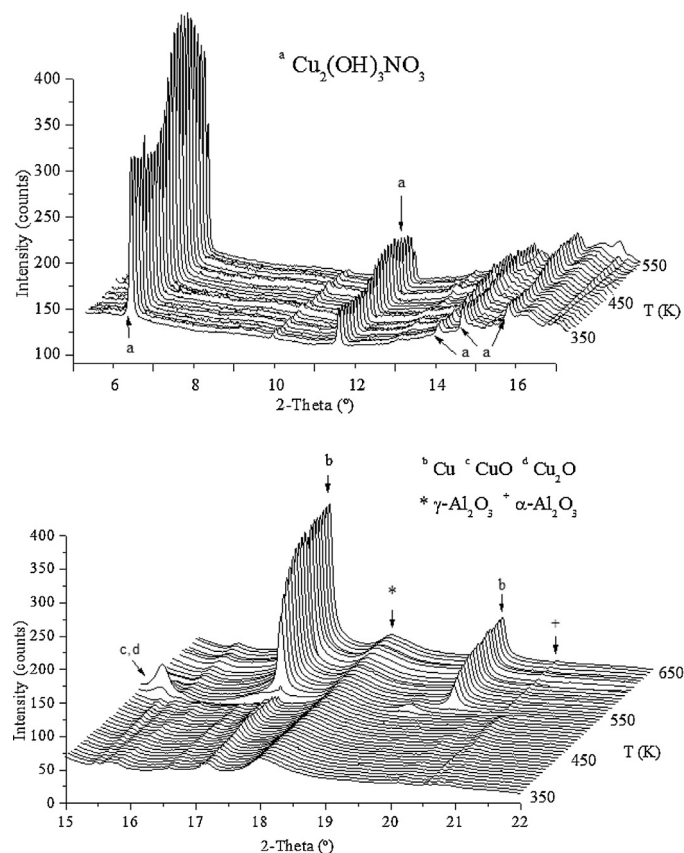


Fig. 2. In situ XRD profiles on the reduction of the copper nitrate precursor impregnated on γ - Al_2O_3 .

when the amount of Cu increases. This indicates that the presence of Cu species enhances the reduction of Ni species [36,37]. In addition, the difference in the position of reduction peaks reported here can be related to the fact that reduction peaks strongly depend on the particle dimension and the interaction strength between metal particles and the support. Previous work dealing with TPR studies on the reduction of Ni–Cu/ γ - Al_2O_3 catalysts suggested that the addition of Cu to Ni precursors can dramatically decrease the reducing temperature of Ni oxides, and might markedly enhance the reducibility of the mixed oxide catalysts [23,38,39]. The promotion effect was stronger as the amount of Cu introduced increased [40–42].

3.1.3. N_2 -physorption

The N_2 -physorption results of the fresh and used samples are depicted in Table 1. The BET surface areas of the fresh samples change between 90 and $111 \text{ m}^2/\text{g}$. The addition of Cu to Ni/ γ - Al_2O_3 catalyst did not affect the BET surface area. For NiCu11 and NiCu12 samples the BET surface area, pore volume and pore size slight decrease after glycerol conversion reaction, suggesting some degree of pore blocking, probably due to carbon deposition.

3.1.4. NH_3 -TPD

The amounts of desorbed ammonia measured by volumetric adsorption for all the samples are shown in Table 2. The surface acidity was calculated as total acidity and expressed per μmol of NH_3 desorbed per gram of sample (Table 2). The γ - Al_2O_3 support presented a total acidity of $182.1 \mu\text{mol}/\text{g}_{\text{sample}}$, which increased to $224.5 \mu\text{mol}/\text{g}_{\text{sample}}$ after Ni incorporation and decreased to $175.4 \mu\text{mol}/\text{g}_{\text{sample}}$ when Cu was added to γ - Al_2O_3 . For the bimetallic catalysts, the addition of Cu produces a decrease of the total

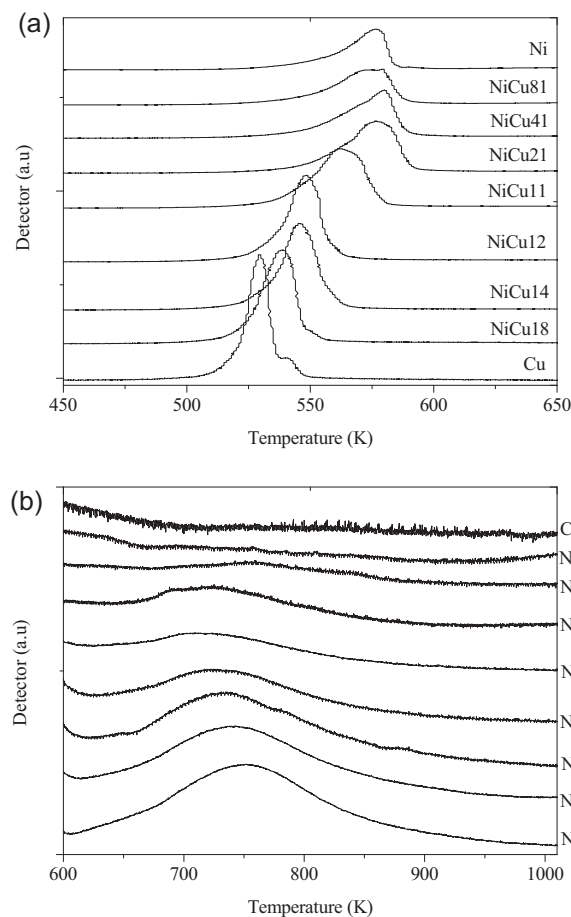


Fig. 3. The TPR patterns of the Ni–Cu/ γ - Al_2O_3 catalysts and the correspondent monometallic samples (a) 450–650 K, and (b) 600–1000 K.

acidity regarding the monometallic Ni sample in the range from 171.8 to $113.5 \mu\text{mol}/\text{g}_{\text{sample}}$.

3.1.5. X-ray diffraction

XRD patterns of the Ni–Cu catalysts were recorded in order to identify the crystalline phases formed after the reduction at 723 K under H_2 flow of the impregnated samples (Fig. 4a). We observed crystallographic phases corresponding to metallic Cu for samples with high amount of Cu and γ - Al_2O_3 phase of the support for all samples. The peaks at around $2\theta = 37.5^\circ$, 45.7° and 66.7° were assigned to γ - Al_2O_3 phase and the peaks at around $2\theta = 43.3^\circ$, 50.4° and 74.1° are associated with metal Cu phase [33,35,38,43–45]. Diffraction peaks of Ni species are not observed in all the XRD patterns. The lack of Ni-related reflections can be attributed to highly dispersed Ni atoms.

Fig. 4c shows the XRD patterns measurements of the monometallic Ni and Cu samples, and bimetallic samples (NiCu11, NiCu12, NiCu14 and NiCu18) in the range $2\theta = 42$ – 54° . The XRD measurements were performed with an internal standard (silicium metallic). It is noticed a slight shift in the diffraction peak of the bimetallic samples to higher 2θ as Ni/Cu atomic ratio increases. Concerning the XRD pattern of the NiCu11 sample, the sharp peak detected at around $2\theta = 43.36^\circ$ is similar to that expected for metal Cu phase ($2\theta = 43.32^\circ$, $a = 3.6150 \text{ \AA}$) although the lattice parameter detected in this case ($a = 3.6111 \text{ \AA}$) appears slightly smaller (Table 2). A possibility in this sense is that such change in the lattice parameter is due to formation of a Ni–Cu alloy which is more enriched in Cu. Based on the Vegard's law [46] the molar fraction of Cu in the NiCu11 sample was calculated to be 0.95, which

Table 1Textural properties of fresh and used 10%Ni–Cu/ γ -Al₂O₃ catalysts.

Sample	Fresh			Used		
	S_{BET} (m ² /g)	Pore volume (cm ³ /g)	Pore size (nm)	S_{BET} (m ² /g)	Pore volume (cm ³ /g)	Pore size (nm)
γ -Al ₂ O ₃	99	0.17	4.54	–	–	–
Ni	108	0.17	4.15	105	0.16	4.15
NiCu81	108	0.16	4.54	89	0.13	4.15
NiCu41	104	0.16	4.54	95	0.14	4.15
NiCu21	105	0.17	4.54	94	0.14	4.15
NiCu11	111	0.18	4.54	82	0.12	4.15
NiCu12	104	0.17	4.54	80	0.14	4.15
NiCu14	104	0.18	4.54	95	0.15	4.15
NiCu18	101	0.18	4.54	94	0.15	4.15
Cu	90	0.16	4.54	98	0.17	4.15

Table 2Physical-chemical properties of 10%Ni–Cu/ γ -Al₂O₃ samples.

Sample	Fresh				Used	
	TPD-NH ₃ ($\mu\text{mol/g}_{\text{sample}}$)	Number of exposed Ni atoms	TPR		Lattice parameter (Å) ^b	TPO (wt.% C)
			450–600 (K)	600–1000 (K)		
γ -Al ₂ O ₃	182.1	–	–	–	–	–
Ni	224.5	9.22×10^{19} (82%) ^a	576	747	3.523 ^c	1.82
NiCu81	146.0	4.16×10^{19} (37%) ^a	575	739	–	0.16
NiCu41	171.8	3.60×10^{19} (32%) ^a	579	729	–	1.18
NiCu21	118.8	2.52×10^{19} (22%) ^a	577	723	–	1.55
NiCu11	128.0	6.97×10^{18} (6.2%) ^a	564	716	3.611	3.76
NiCu12	107.1	0	547	715	3.614	7.16
NiCu14	113.5	0	545	–	3.613	2.72
NiCu18	114.7	0	539	–	3.615	4.26
Cu	175.4	0	529	–	3.615 ^c	0.34

^a Values in the brackets are dispersion.^b Lattice parameter determined by XRD analysis.^c Theoretical values for Ni and Cu.

suggests that a small fraction of Ni is alloying with Cu [47]. The lattice parameters of the samples are plotted in Fig. 4d with respect to the Ni/Cu atomic ratio. The discrepancy of calculated lattice parameters from those expected by the Vegard's law (dots line) reveal that our Ni–Cu samples are not a total intermetallic alloy.

3.1.6. HRTEM

The morphology and the metal particle size of the as-prepared Ni–Cu catalysts were characterized by HRTEM. Fig. 5a shows a low magnification TEM image of the monometallic Cu catalyst. It shows very small crystallites of the γ -Al₂O₃ support along with well-dispersed small Cu nanoparticles with higher electron contrast. It must be added that XRD is often compared to the microscopy techniques to characterize particle sizes. TEM images directly visualize irregularities such as variations of the particle shape or the presence of some considerably larger or smaller particles. TEM allows the best estimation of the degree of homogeneity of a given sample. Fig. 5b shows a high resolution TEM image with several Cu nanoparticles, which measure about 1.5–2 nm in diameter. The lattice-fringe image allows for a proper identification, the planes at 2.1 Å correspond to (1 1 1) planes of metallic Cu. For monometallic Ni catalyst TEM image shows Ni particles well distributed over the γ -Al₂O₃ support (Fig. 5c). A HRTEM image is depicted in Fig. 5d, where the inset corresponds to the area enclosed in the square. The lattice spacing at 2.0 Å corresponds to the (1 1 1) planes of Ni metal and the Ni particle size is about 4–6 nm in diameter. For NiCu11 catalyst, particles with higher electron contrast correspond to metal particles, which are very well distributed over the γ -Al₂O₃ support (Fig. 5e). An HRTEM image of one of these particles is shown in Fig. 5f. The Fourier Transform image of the area selected shows spots at 1.8 Å, which correspond to (2 0 0) planes of Ni, Cu, or an alloy. The metal crystallite is oriented along the [1 0 0]

crystallographic direction. Given the similarities of the lattice parameters of Ni and Cu it is difficult to distinguish between them, so it is not possible to conclude by this technique if Ni–Cu alloy particles are present or if Ni and Cu occur separately. Nevertheless, the particle size distribution of the metal particles is mostly within the range of 3–5 nm in diameter, which lies within those of monometallic Cu and Ni catalysts. Another HRTEM image with various metal particles showing lattice fringes is shown in Fig. 5g. Lattice fringes at 1.8 and 2.1 Å are identified, which correspond to (2 0 0) and (1 1 1) planes.

3.1.7. H₂-chemisorption

Table 2 shows the number of exposed and dispersion of Ni atoms determined by H₂-chemisorption. The monometallic Ni sample has the highest number of exposed Ni atoms (9.22×10^{19}) which decreases as the Cu loading increases. The exposed Ni atoms change from 4.16×10^{19} for NiCu81 to 6.97×10^{18} for NiCu11 sample. The strongly chemisorbed hydrogen is not observed for the monometallic Cu catalyst. For the catalysts NiCu12, NiCu14, NiCu18 the number of exposed Ni atoms was also indistinguishable. It is noticed that the H₂ chemisorption ability of the bimetallic catalysts decreases upon Cu addition [48]. These results clearly suggest that Cu is the predominant component in the surface of Ni–Cu samples after preparation, in agreement with the literature [49].

3.1.8. XPS

The binding energy, the surface atomic percentages of Cu and Ni, and the XPS atomic ratios of Ni/Al and Cu/Al for all Ni–Cu catalysts are given in Table 3. The monometallic Cu catalyst shows the Cu 2p_{3/2} main peak at 931.8 eV. The monometallic Ni sample shows the Ni 2p_{3/2} main peak at 854.9 eV. There is not a significant change in these binding energies when a part of Cu is replaced

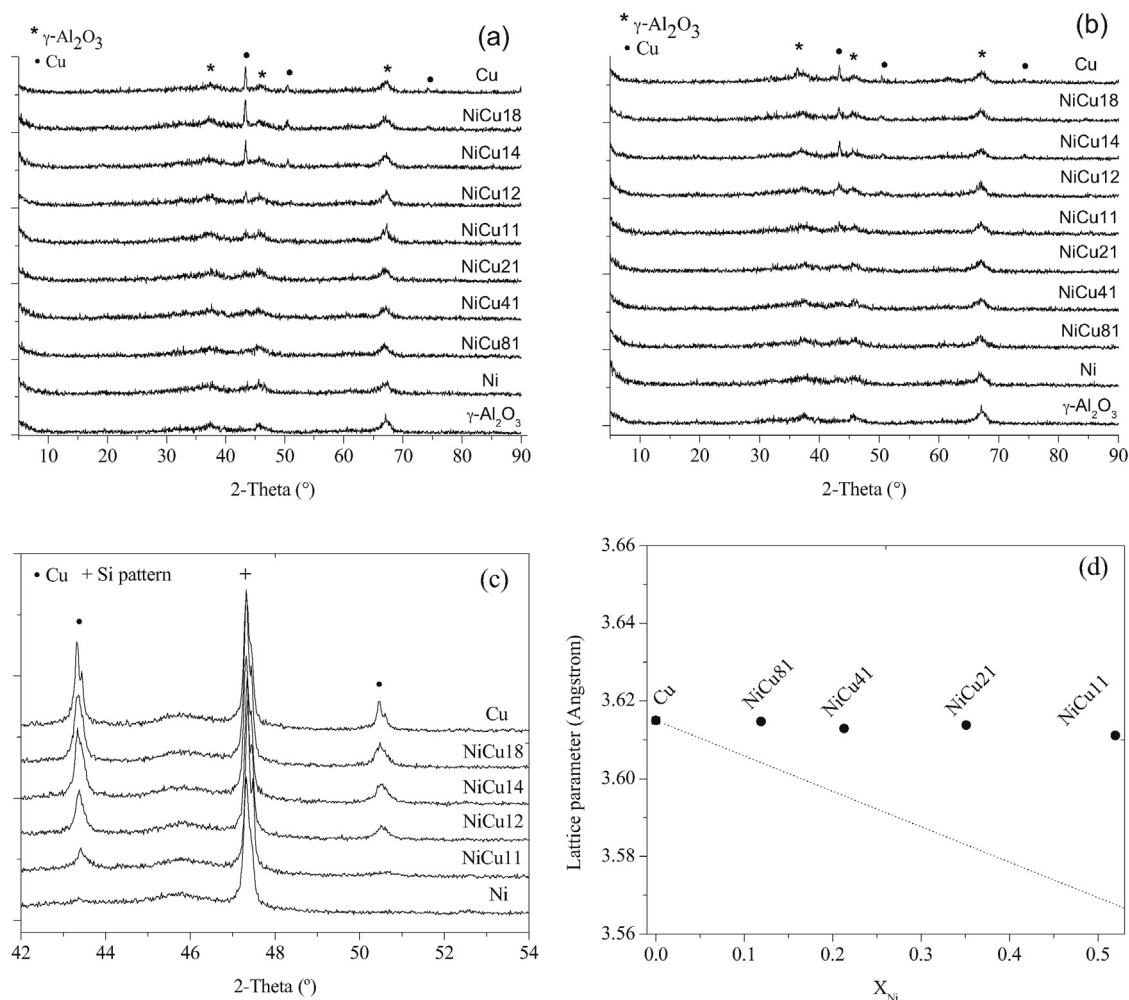


Fig. 4. X-ray diffraction patterns (a and c) fresh and (b) spent supported Ni–Cu/ γ - Al_2O_3 catalysts, (d) lattice parameter of the samples versus Ni/Cu ratio.

by Ni. The Ni/Al ratio decreases as the amount of Cu increases. On the other hand the Cu/Al atomic ratio increases as the copper content increases. In addition, the ratio of the intensity of the Ni $2p_{3/2}$ peak to that of the Cu $2p_{3/2}$ peak decreases as the Cu content in the sample increases, indicating that the external boundary surfaces of the samples are enriched by Cu. The Cu catalyst surface enrichment is also suggested by the H_2 chemisorption (Table 2) results, where the amount of irreversible hydrogen chemisorbed decreases as the Ni/Cu atomic ratio decreases. The present results are consistent with previous results on bimetallic Ni–Cu systems, where surface segregation of Cu is predominantly reported. This is justified on the basis of thermodynamics because the lower heat of sublimation (i.e., lower surface free energy) of Cu compared to Ni

leads to Cu occupying the surface sites of the bimetallic particles [49]. Pure Cu exhibits no strong chemisorption of hydrogen.

3.1.9. FTIR of adsorbed CO

Nickel in different oxidation states can be distinguished by the vibration frequencies of adsorbed CO. In general, adsorption of CO at RT on metallic Ni can be divided into two groups: (i) reversible and (ii) irreversible adsorbed. The irreversible adsorption is attributed to two different species: linear and bridge-bound CO [50]. The high frequency band at $2100\text{--}2000\text{ cm}^{-1}$ can be assigned to linearly adsorbed CO on metallic Ni. The low frequency band at $2000\text{--}1800\text{ cm}^{-1}$ is attributed to CO adsorbed in two or three fold bridge configuration on metallic Ni [51].

Table 3

XPS experimental binding energies, surface atomic percentage and atomic ratio of 10%Ni–Cu/ γ - Al_2O_3 samples reduced at 723 K.

Sample	Binding energy (eV)			Surface atomic (%)		Atomic ratio (XPS)			Ni/Cu (theoretical)
	Cu $2p_{3/2}$	Ni $2p_{3/2}$	Al 2p	Cu	Ni	Ni/Al	Cu/Al	Ni/Cu	
Ni	–	854.9	73.1	–	8.11	0.088	–	–	–
NiCu81	932.3	855.1	73.4	3.25	8.90	0.101	0.037	2.74	8
NiCu41	932.0	855.0	73.7	5.12	6.47	0.073	0.058	1.26	4
NiCu21	931.4	854.4	72.9	6.47	4.99	0.056	0.073	0.77	2
NiCu11	931.8	854.6	73.0	5.85	3.00	0.033	0.064	0.51	1
NiCu12	932.4	855.1	72.8	6.61	1.33	0.015	0.072	0.20	0.5
NiCu14	931.7	855.1	73.1	7.05	1.07	0.012	0.077	0.15	0.25
NiCu18	931.9	855.6	73.7	15.5	0.72	0.009	0.186	0.05	0.125
Cu	931.8	–	73.8	14.3	–	–	0.167	–	–

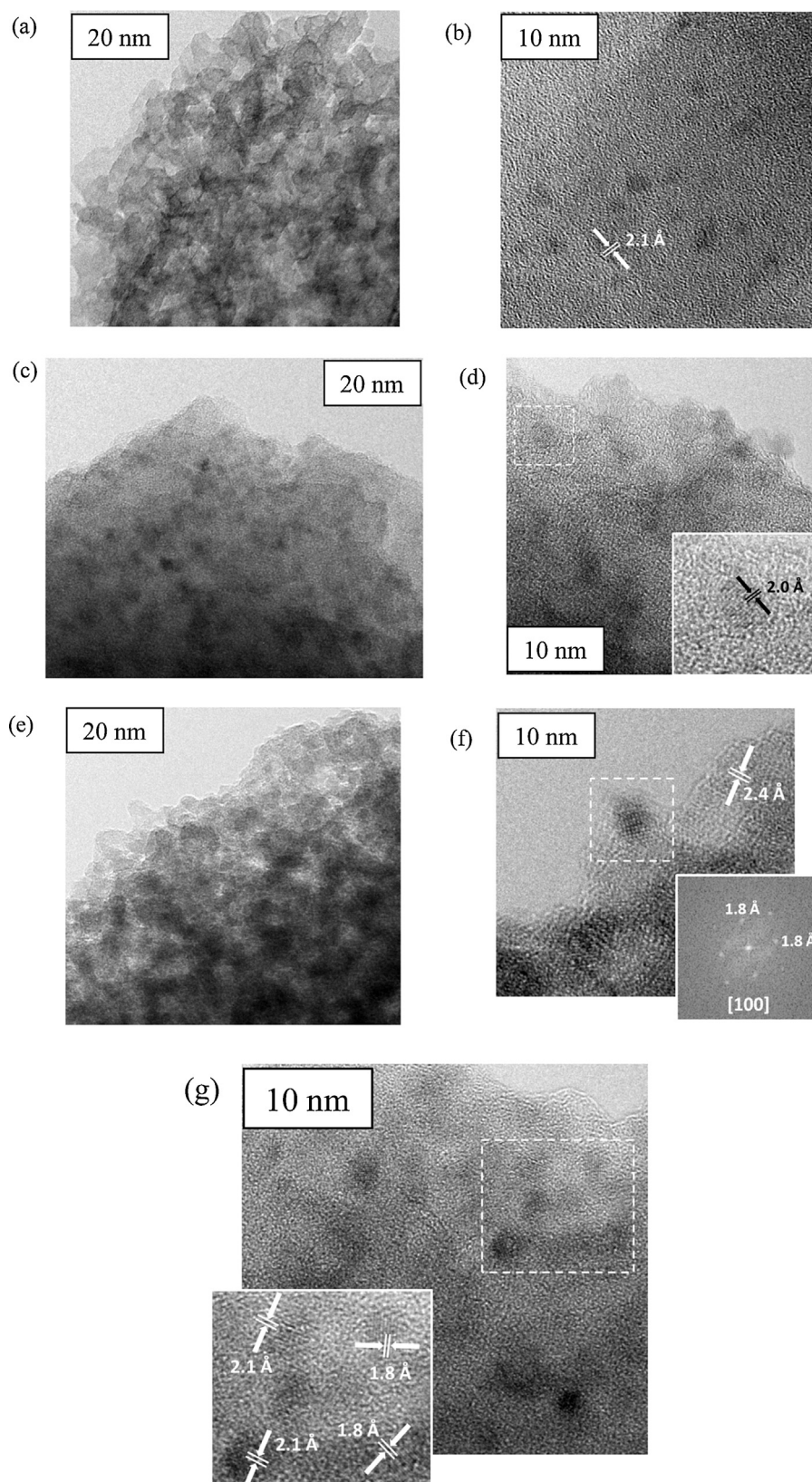


Fig. 5. HRTEM images of the fresh (a and b) monometallic Cu, (c and d) monometallic Ni, and (e–g) bimetallic NiCu11 samples reduced at 723 K.

Fig. 6 shows the IR spectra of adsorbed CO on Ni–Cu samples at RT after reduction at 723 K. The spectra displayed were obtained after different CO doses and evacuation in order to eliminate the gas phase species.

On the monometallic Ni sample, the observed band at 2132 cm^{-1} is attributed to CO polarized by Ni^{+2} ions [50]. The observed bands at 2056 and 2037 cm^{-1} can be related to CO linearly bonded to the Ni surface [51] in agreement with Blackmond

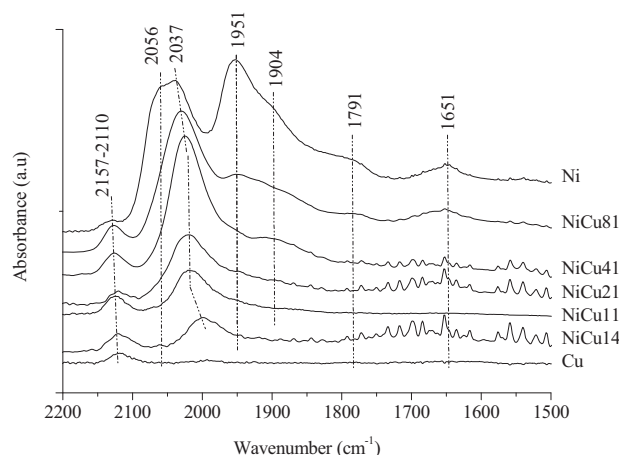


Fig. 6. Infrared spectra of reduced catalysts after evacuation of CO.

and Ko [52]. The bands $1952\text{--}1892\text{ cm}^{-1}$ can be assigned to CO molecules bridge-bonded to Ni atoms. The bands below 1890 cm^{-1} are attributed to Ni_3CO and Ni_4CO species [53].

The addition of Cu to the Ni catalysts (Fig. 6) resulted in the elimination of CO molecules bridged-bonded to metallic Ni (geometric effect) as the Ni/Cu atomic ratio decreased. Additionally, the IR band position of linearly adsorbed CO molecules on Ni red shifted. The shift to lower wavenumber was about 38 cm^{-1} . This may indicate an interaction of Ni with neighboring Cu atoms (electronic effect).

The monometallic Cu catalyst presents a band at 2132 cm^{-1} ascribed to CO adsorbed on Cu^+ species [49,54]. With increasing Ni/Cu atomic ratio a slight shift to higher wavenumbers can be observed. This suggests an interaction of Cu^+ species with Ni.

3.1.10. XANES

Fig. 7 shows XANES spectra for reduction of impregnated samples (Cu, Ni, and Ni–Cu) with 5% H_2 in He. For the monometallic Ni catalyst (Ni K-edge), the white line (WL) is not affected by the increase in reduction temperature between RT and 700 K, indicating that the Ni content is still oxidized below 700 K (Fig. 7a). Between 700 and 973 K, the WL decreases and 50% of the Ni oxide is converted to metallic Ni at 800 K (Fig. 7c). On the bimetallic NiCu11 sample the WL starts to change at around 350–400 K (Fig. 7b). In this case 50% of Ni oxide is reduced at about 750 K (Fig. 7d). The decrease in the reduction temperature observed in the bimetallic sample suggests an interaction between Ni and Cu [49] and these results are in good agreement with TPR (Fig. 3).

The XANES results taken on K-edge of the Cu for monometallic Cu and NiCu11 samples are shown in Figs. 7e and f. Below 540 K Cu is completely in +II oxidation state (Tenorite: CuO) in both samples. At this temperature it is observed that 40% Cu species in the monometallic Cu sample are as Cu(I) oxide (Cuprite: Cu_2O), 30% as metallic Cu and around 30% remaining as CuO (Fig. 7g). On the other hand in the NiCu11 sample it is observed that CuO completely disappears, at 540 K the Cu species are present in two phases: 35% as Cu_2O and 65% as metallic Cu (Fig. 7h). In the final reduction condition (973 K) it is observed Cu phases distributed as follows: 20–25% as metallic Cu, 80% as Cu_2O phase and CuO disappeared completely in the monometallic Cu sample (Fig. 7g). On the other hand, in the bimetallic sample the Cu species present are: 10% as Cu_2O and 90% as metallic Cu (Fig. 7h), suggesting an interaction between Cu and Ni species.

3.2. Hydrogenolysis of glycerol

The main products in the condensable phase during conversion of glycerol at 573 K under atmospheric pressure were:

hydroxyacetone, pyruvaldehyde, lactide, lactic acid, acetic acid, pyruvic acid, EG, acetaldehyde, and traces of 1,2-PDO and furan derivatives. Previous works about glycerol conversion reported that the furan compounds are the result of a catalytic cyclisation of hydroxyacetone [55]. The major products detected in the gas phase were CH_4 , acetaldehyde and traces of acetone. The selectivity of hydrogenolysis products such as CH_4 and acetaldehyde and dehydration products (such as hydroxyacetone) were dependent on the Ni/Cu atomic ratio.

The glycerol conversion versus time of reaction for the Ni–Cu catalysts is shown in Fig. 8. For the samples with high amount of Ni (Ni, NiCu81, NiCu41 and NiCu21) the glycerol conversion was about 100% over 6 h of reaction indicating high stability of the catalysts. However, the glycerol conversion decreases with time for samples enriched with Cu, indicating high deactivation for samples NiCu11, NiCu12, NiCu14, NiCu18 and Cu (Fig. 8). It is clear that when the Cu content increased a decrease in glycerol conversion with time on stream is observed. The deactivation was more pronounced for the NiCu14 and NiCu18 catalysts (Table 4). The glycerol conversion for the monometallic Cu sample dropped from 93% to about 60%. It suffered less deactivation than the bimetallic samples with higher content of Cu.

The selectivity profiles obtained for the Ni–Cu catalysts are shown in Fig. 9. It can be seen that the selectivity to CH_4 is practically 100% on Ni, NiCu81, and NiCu41 catalysts. Our previous work [22] revealed that the increase in the total number of exposed Ni atoms and the degree of reduction of the NiO species increases the selectivity to CH_4 affecting the catalytic stability. Further increase in Cu content causes a decrease in the selectivity to CH_4 . The opposite behavior is observed on selectivity to dehydration–dehydrogenation products such as hydroxyacetone and pyruvaldehyde which increases with increasing Cu content. The production of CH_4 was totally suppressed in the monometallic Cu sample. Thus, the results show that selectivity to CH_4 decreases progressively when the Ni/Cu atomic ratio decreases. The effect of addition of Cu on Ni/ Al_2O_3 can be observed in Table 4. The selectivity to hydroxyacetone is close to 30% for NiCu11, NiCu12, NiCu14, and NiCu18 catalysts while on Cu is about 40% suggesting that the addition of high amount of Cu on Ni favors the dehydration of glycerol to hydroxyacetone. Similar behavior is observed to formation of pyruvaldehyde. The production of lactide preferably occurs on NiCu11, NiCu12, NiCu14, and NiCu18 catalysts and it occurs in less extension on Cu/ Al_2O_3 . Thus, it can be remarked that the incorporation of Cu on Ni decreases the C–C bond linkage markedly. This indicates that the metal components clearly are not isolated from each other on the support. The activity results data provide also strong evidence of interaction between Cu and Ni. This interaction is reinforced by our characterization techniques.

3.3. Reaction pathway

The monometallic Ni sample promotes total deep hydrogenolysis of glycerol to CH_4 (Table 4). The deep hydrogenolysis route is progressively suppressed when the Ni/Cu atomic ratio decreases. EG was detected on NiCu11 and NiCu12 catalysts while acetaldehyde was detected on NiCu81, NiCu41, NiCu21, NiCu11, and NiCu12 samples. Acetaldehyde afterwards produce acetic acid probably by a base catalyzed reaction taking in account that the alumina support has a basic character. Dehydration and dehydrogenation products such as hydroxyacetone, pyruvaldehyde, lactide and pyruvic acid started to be produced when the Cu content increased. In the monometallic Cu sample the hydrogenolysis products such as CH_4 , EG, acetaldehyde and acetic acid were totally suppressed.

Hydroxyacetone, pyruvaldehyde and lactic acid were used as reactants under the same operation conditions performed for the catalytic conversion of glycerol over the monometallic Cu catalyst

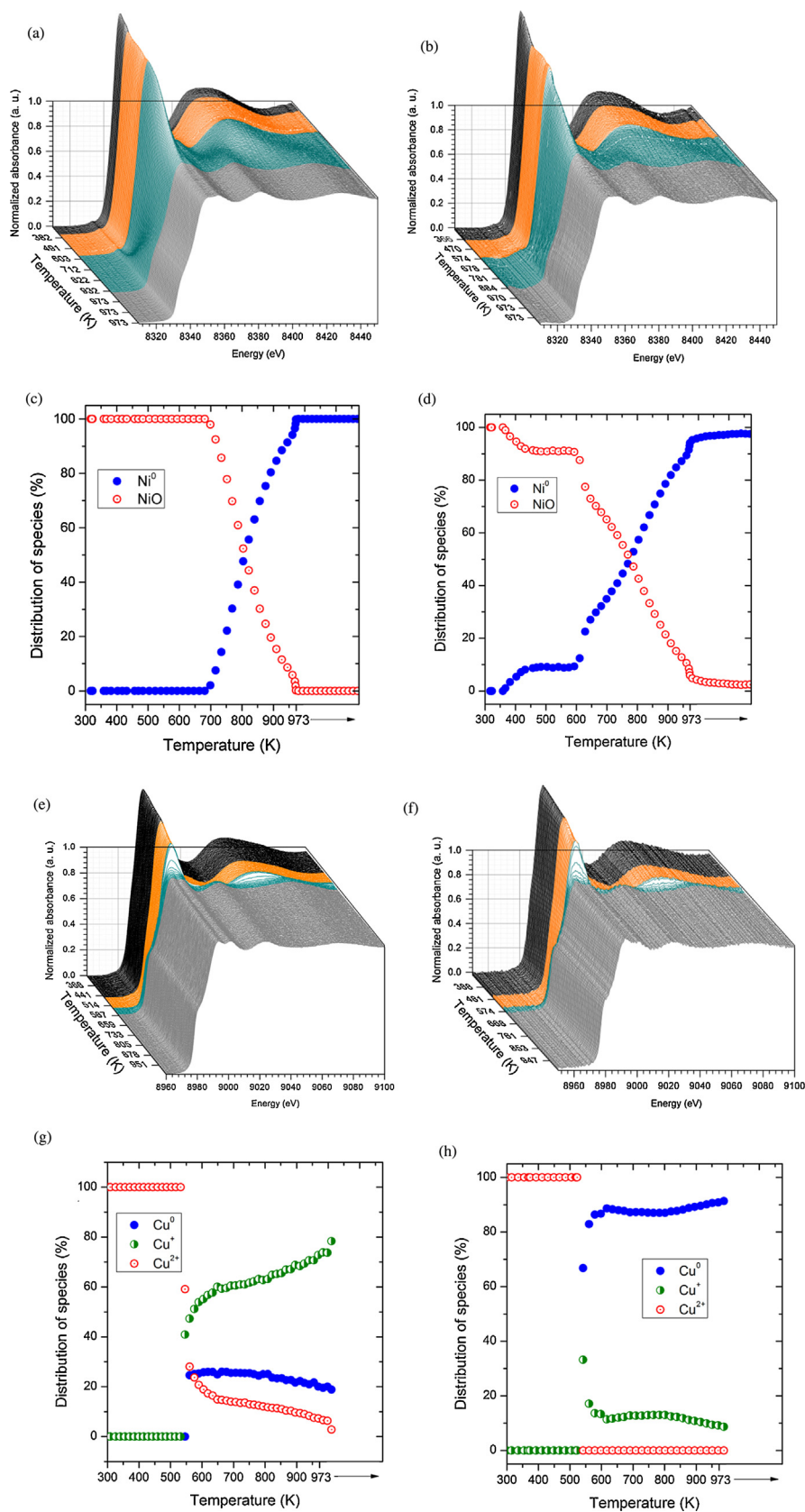


Fig. 7. XANES spectra at the Ni K-edge of the (a) monometallic Ni and (b) NiCu11 samples, amount of reduced versus oxidized Ni species for the (c) monometallic Ni and (d) NiCu11 samples, Cu K-edge of the (e) monometallic Cu and (f) NiCu11 samples, amount of reduced versus oxidized Cu species for the (g) monometallic Cu and (h) NiCu11 samples, during reducing in 5% H₂ in He.

Table 4

Product selectivity in the conversion at 573 K of several main products from the catalytic conversion of glycerol at 4 h of reaction.

Column 1	Column 2	Column 3	Column 4	Column 5	Column 6	Column 7	Column 8	Column 9	Column 10
Catalyst	Ni	NiCu81	NiCu41	NiCu21	NiCu11	NiCu12	NiCu14	NiCu18	Cu
Conversion (%)	100	98.8	99.6	99.0	56.3	74.5	43.1	42.8	67.4
Selectivity (%)									
Methane	100	92.2	92.4	79.3	3.69	5.65	3.12	0.15	–
Hydroxyacetone	–	3.88	2.56	5.25	30.3	34.5	32.3	28.7	39.6
Pyrvaldehyde	–	2.77	1.55	2.38	16.2	17.6	15.5	16.0	33.8
Acetic acid	–	0.53	2.06	3.41	1.07	0.55	–	–	–
Pyruvic acid	–	–	–	–	3.59	2.62	2.90	4.05	5.98
Lactic acid	–	–	–	–	–	–	–	–	2.77
Lactide	–	–	–	–	42.9	31.6	46.1	51.1	17.8
Ethylene glycol	–	–	–	–	1.89	2.06	–	–	–
Acetaldehyde	–	0.61	1.41	9.67	0.24	5.24	–	–	–

Table 5

Product selectivity in the conversion at 573 K of several main products from the catalytic conversion of glycerol with monometallic Cu sample at 4 h of reaction.

Column 1	Column 2	Column 3	Column 4	Column 5	Column 6	Column 7
Reactant	Glycerol	Glycerol	Glycerol	Hydroxyacetone ^a	Pyrvaldehyde	Lactic acid
Molar ratio H ₂ /reactant	10	0 ^a	10 ^b	10	10	10
Conversion (%)	67.4	47.7	60.8	0.95	38.3	97.9
Selectivity (%)						
Acetic acid	–	–	–	–	6.41	–
Hydroxyacetone	39.6	23.9	41.7	–	28.9	–
Lactic acid	2.77	–	5.11	9.45	17.8	–
Lactide	17.8	27.7	20.6	57.9	28.9	7.17
Pyrvaldehyde	33.8	41.8	27.8	32.6	–	4.07
Pyruvic acid	5.98	6.60	4.78	–	17.9	80.7
Acetaldehyde	–	–	–	–	–	8.06
Mass balance ^c (%)	98	84	94	100	100	95

^a Argon atmosphere.^b CuO catalyst.^c TOC, HPLC and CG analysis.^{*} 2 h of reaction.

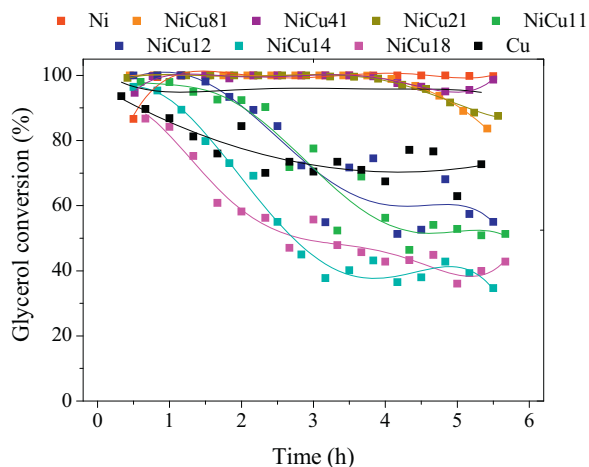
in order to investigate the role of the Cu in the reaction pathway. The main products obtained when hydroxyacetone was employed as reactant (column 5, Table 5) were lactide, pyrvaldehyde and lactic acid. However, the conversion of hydroxyacetone was less than 1.0% indicating poor catalytic activity of Cu. The strong deactivation observed can be attributed to catalytic cyclization of hydroxyacetone [12]. Indeed, in this case, the monometallic Cu catalyst suffered strong deactivation at only 1 h of reaction. This fact suggests that the dehydration of glycerol may strongly contribute with the carbon deposition on the catalyst surface [55]. From our previous work [22], the conversion of hydroxyacetone with the Ni/γ-Al₂O₃ catalyst was about 16% and the major product was lactic acid with

selectivity of 61%. Differently of Cu/γ-Al₂O₃, selectivity of 14% to CH₄ was observed on Ni/γ-Al₂O₃ during hydroxyacetone reaction indicating the C–C bond breaking on Ni in our previous work [22].

During catalytic conversion of pyrvaldehyde on Cu/γ-Al₂O₃ hydroxyacetone, lactic acid, lactide, pyruvic acid and acetic acid were the major products with selectivity of 28.9%, 17.8%, 28.9%, 17.9% and 6.41%, respectively (column 6, Table 5). These results suggest that hydroxyacetone may be formed from the hydrogenation of pyrvaldehyde. When lactic acid was employed as reactant (column 7, Table 5), the main products obtained were lactide, pyrvaldehyde, pyruvic acid and acetaldehyde.

Table 5 also shows that when the monometallic Cu catalyst was previously calcined at 723 K instead of reduced, the glycerol conversion (60.8%, column 4) was slight lower than that observed under H₂ flow (67.4%, column 2). This suggests that dehydration and dehydrogenation of glycerol can also occur on oxidized Cu species. In addition, the conversion of glycerol using the monometallic Cu catalyst under Ar flow revealed a glycerol conversion of 47.7% (column 3, Table 5) which is lower than that observed under H₂ flow.

The results above were used to propose a general reaction pathway of the glycerol conversion on Ni–Cu bimetallic catalysts (see Scheme 1). Details about the reaction pathway on Ni/γ-Al₂O₃ were discussed in our previous work [22]. As the Cu content in the catalysts increases the reaction pathway is conducted to the products inside to the dashed line of the rectangle. Glycerol is consumed either by hydrogenolysis to CH₄ or dehydration to form hydroxyacetone which is dehydrogenated to pyrvaldehyde. The dehydration route becomes more pronounced when Cu content in the samples increases. Pyrvaldehyde can be hydrogenated to form hydroxyacetone. Acetaldehyde and the CH₄ can be obtained from the catalytic C–C bond cleavage of hydroxyacetone [56]. In addition pyrvaldehyde can be converted to lactic acid either via

**Fig. 8.** Catalytic performances for Ni–Cu/γ-Al₂O₃ catalysts in function of time of reaction.

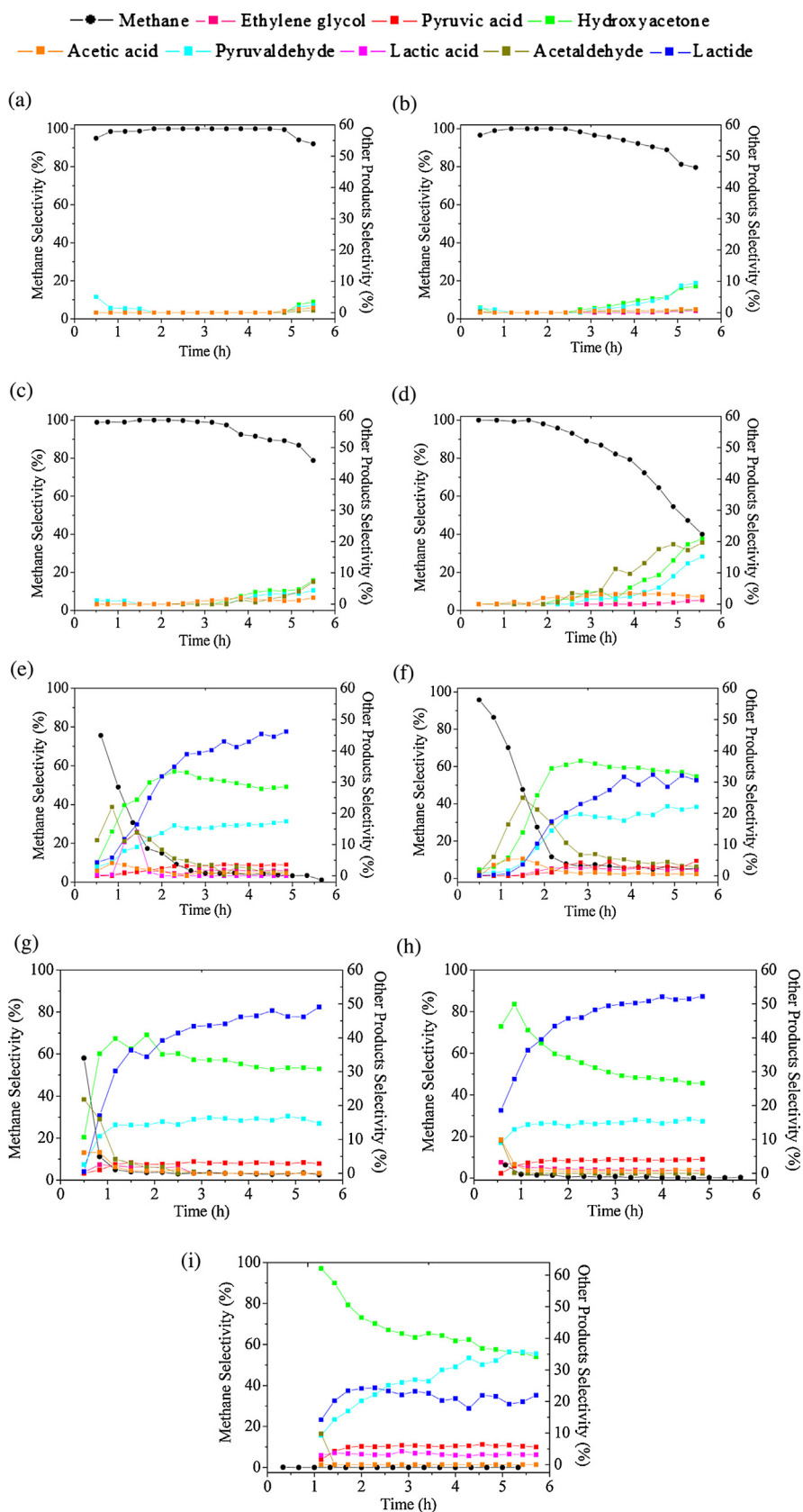
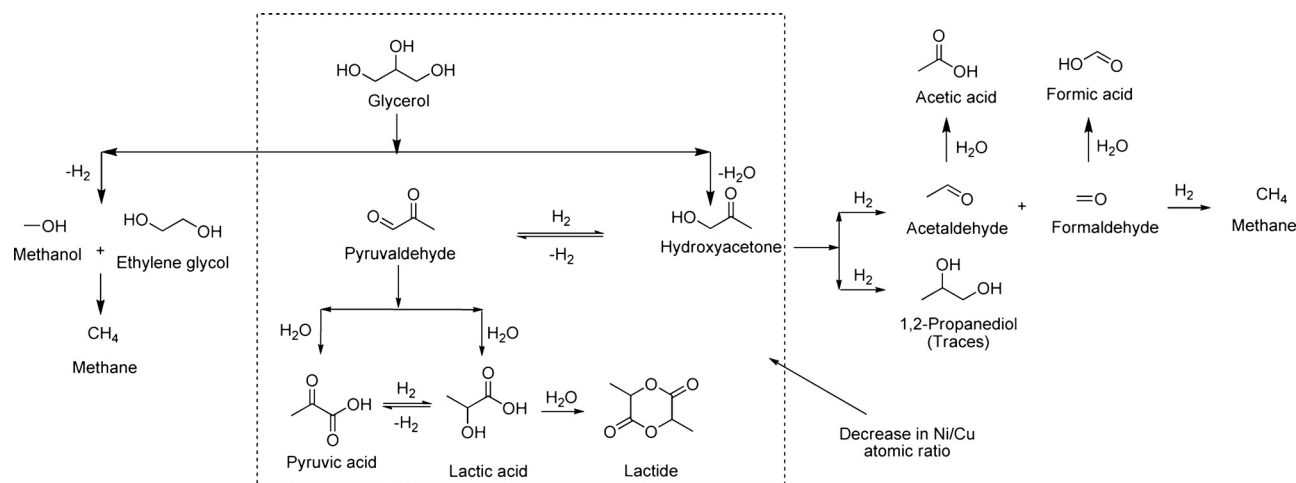


Fig. 9. Time-on stream product selectivity in glycerol conversion over (a) Ni, (b) NiCu81, (c) NiCu41, (d) NiCu21, (e) NiCu11, (f) NiCu12, (g) NiCu14, (h) NiCu18 and (i) Cu.



Scheme 1. Proposed reaction pathway for glycerol conversion over Ni-Cu/ γ -Al₂O₃ catalysts illustrating the main reaction products.

a Cannizzaro reaction [18] or via oxidation to pyruvic acid which can further hydrogenate forming lactic acid in a reverse reaction. Finally the lactic acid undergoes dimerization to form lactide.

3.4. Used samples

Catalytic deactivation was observed in the glycerol conversion as is shown in Fig. 8. The N₂-physisorption (Table 1) reveals a slight decrease in the BET area, pore volume and pore size compared to the fresh samples especially for the bimetallic samples with higher content in Cu. This may suggest carbonaceous deposition during the reaction. XRD results for the used Ni-Cu samples (Fig. 4b) did not reveal changes in the structure of the materials. Raman spectra (data not shown) in the range of 1100 to 2000 cm⁻¹ displayed two main bands D and G [47] ascribed to carbon species. According to previous works [57–59], the D-band is associated to non-deactivating carbon (amorphous carbon) and the G-band is related to deactivating carbon (graphitic carbon). The carbon deposition on used Ni-Cu samples was determined by TPO as shown in Table 2. The monometallic Ni sample showed 1.82 wt.% of carbon deposited and the monometallic Cu sample presented 0.34 wt.%. For the bimetallic samples, it can be seen an increase in carbon deposition in the samples with higher Cu content such as 7.16 wt.% for NiCu12, 2.72 wt.% for NiCu14 and 4.26 wt.% for NiCu18 samples. This indicates the direct involvement of Cu species in the dehydration of glycerol. The dehydration route markedly contributes to the carbon deposition on the catalysts as noted by previous works leading to the observed deactivation [56]. The formation of carbon deposits during dehydration reaction of glycerol may result from consecutive reactions of glycerol, like oligomerization on acidic catalyst surface sites and/or side reactions between dehydrated products like hydroxyacetone [55]. In fact, our results show that the glycerol dehydration route dominates over the hydrogenolysis when the Cu content increases and higher content of deposited carbon was observed in these samples (e.g. NiCu11, NiCu12, NiCu14, and NiCu18). On the contrary, bimetallic catalysts with small amount of Cu such as NiCu81 are stable during glycerol conversion. Interestingly, the monometallic Ni catalyst was very stable during glycerol reaction compared to Ni catalyst used in our previous work [22]. The catalysts used in the present work were prepared by wet impregnation while the Ni catalyst used in previous work [22] was prepared by incipient wetness impregnation. The wet impregnation resulted in a higher amount of Ni exposed atoms suggesting an effect of the Ni particle size on the glycerol reaction.

4. Discussion

The dependence of the adsorption properties and the glycerol hydrogenolysis was evaluated by the bimetallic Ni-Cu system. Our results demonstrate the effects on addition of Cu into Ni/ γ -Al₂O₃ on glycerol conversion and selectivity as well as adsorption properties.

The bimetallic Ni-Cu system is very well distributed on the γ -Al₂O₃ support as revealed by HRTEM (Fig. 5). In addition, the XRD (Fig. 4d) analysis revealed that the amount of intermetallic alloy in the Ni-Cu system was very poor. Small amounts of Ni-Cu alloy were formed on Ni-Cu catalysts.

Evidence that the surface compositions of the Ni-Cu catalysts are different from bulk compositions was provided by H₂ chemisorption data (Table 2) and XPS analysis (Table 3). XPS results show that Cu is enriched on the catalyst surface. In addition, the number of exposed atoms of metallic Ni determined by H₂ chemisorption declined progressively when the Ni/Cu atomic ratio decreases (Table 2). This indicates that Cu is recovering the Ni particles.

TPR (Fig. 3) and XANES (Fig. 7) results revealed a considerably lower reduction temperature of NiO in the bimetallic catalysts compared to the monometallic one (Figs. 3 and 7). This phenomenon suggests that there is an interaction between Cu and Ni species in the catalysts.

The results of glycerol conversion at 573 K show that the addition of Cu into Ni/ γ -Al₂O₃ plays an important key on the selectivity. In fact, a continuous decline is observed in the deep hydrogenolysis route as the Ni/Cu atomic ratio decreases. The CH₄ production sharply decreases by the addition of small amounts of Cu (NiCu81 sample), and it continues to decrease with increasing Cu content over the whole range of the Ni/Cu atomic ratios. As a result higher selectivity toward dehydration products such as hydroxyacetone is observed (Table 4). Selectivity profiles of CH₄ and dehydration products (pyruvaldehyde and hydroxyacetone) versus the total number of exposed Ni atoms are shown in Fig. 10a. Higher the total number of exposed Ni atoms higher is the CH₄ selectivity. When small amount of Cu was added such as in the NiCu81 sample a decrease of 45% of the total number of exposed Ni atoms was observed (Table 2). This is reflected in the increase of the dehydration products (Table 4).

The effect of Cu on Ni/ γ -Al₂O₃ observed here can be attributed to geometrical effect and/or change in electronic properties. The geometric effect would affect the number of Ni sites available for adsorption. The hydrogen chemisorption (Table 2) results suggest that Cu is the predominant component in the surface of the catalyst as the Ni/Cu atomic ratio decreases. Cu progressively covers the Ni

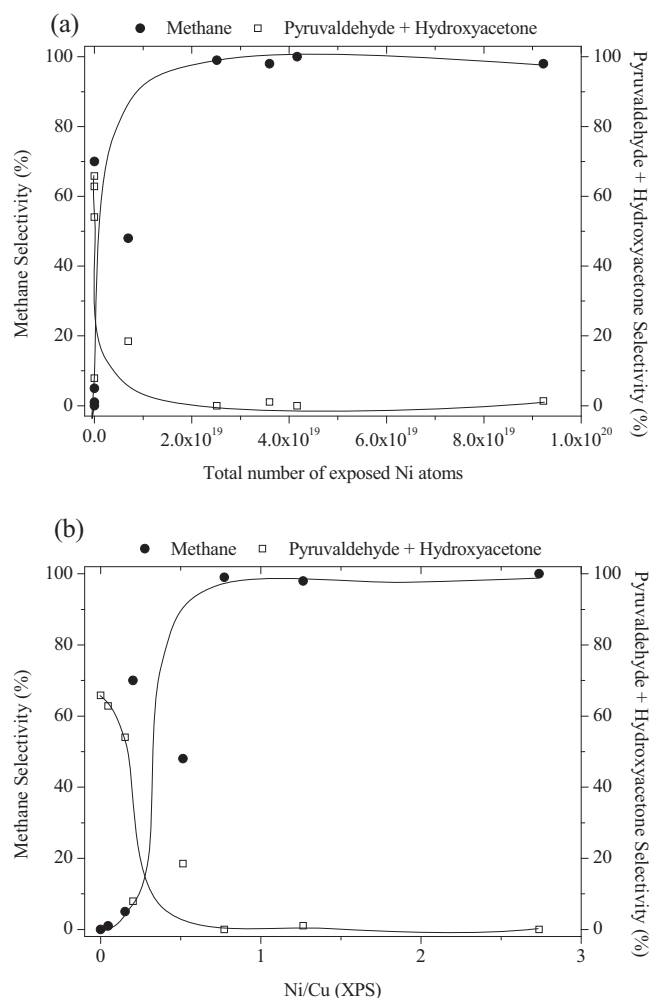


Fig. 10. Dependence of the product selectivity with the total number of exposed Ni atoms in the catalytic conversion of glycerol.

atoms, which was further reinforced by our XPS results (Table 3). As already mentioned, the chemisorption and XPS results suggest that Cu tends to cover the Ni surface. In this regards the activity of Ni atoms toward CH_4 formation is greatly affected as illustrates in Fig. 10b. This effect may be explained by a geometrical effect of dilution of the active hydrogenolysis Ni sites by the presence of Cu atoms. Sinfelt [60] has also observed dramatic activity losses in the ethane hydrogenolysis on Ni when small amounts of Cu are added to the catalyst. On the other hand, lower effects were observed on the same Ni–Cu samples for the dehydration of cyclohexane [61,62]. Thus, our results are in good agreement with the literature.

The geometrical effect is clearly noted by the FTIR of adsorbed CO results (Fig. 6) revealing the progressive elimination of CO molecule bridge bounded to Ni atoms which are observed at the low frequency band $2000\text{--}1800\text{ cm}^{-1}$. In this respect, the active Ni sites for rupture of C–C bond of glycerol may require a large ensemble of atoms. Adjacent Ni atoms on the catalyst surface can form suitable ensemble for the hydrogenolysis route. The probability of finding a suitable array of active Ni atoms to accommodate the reactive molecule may greatly decreases when Cu is dispersed on the Ni catalyst surface. In this way, the decline in the CH_4 production during glycerol reaction clearly reflects an effect of coverage of Ni sites by Cu sites. By contrast, the sites for dehydrogenation and dehydration routes are less sensitive to coverage of the surface by Cu. This was reinforced by the presence of CO molecule linearly bounded to one Ni atom in all range Ni/Cu studied (Fig. 6).

Electronic modification of Ni by the presence of Cu are shown by XANES results (Fig. 7). The observed lower reduction temperature of NiO in the bimetallic catalyst compared to the monometallic one suggests an electronic interaction. According to Pauling [63] Cu has the effect of decreasing the percentage of the d-character of Ni, and thus it can cause an inhibition of C–C bond rupture of glycerol. This electronic effect was observed on Ni–Cu/ $\gamma\text{-Al}_2\text{O}_3$ catalysts during the glycerol conversion. Another potential evidence for the electronic effect is supported by the FTIR of CO adsorption. Upon addition of Cu to Ni species, there is a red shift of approximately 38 cm^{-1} . The CO stretching vibration is predicted to shift from pure Ni as compared to the bimetallic Ni–Cu sample according the Blyholder's scheme [64].

Our results reveal that the geometrical effects are dominant and smaller effects can be attributed to an electronic modification of Ni by the presence of Cu. It is clear that the presence of the Group IB metal such as Cu with the Group VIII metal such as Ni led to inhibition of the rupture of the C–C bond of glycerol. This line of reasoning leads to the expectation that the presence of the Cu markedly inhibit the hydrogenolysis activity of the Ni rendering more selectivity for dehydrogenation and dehydration of glycerol.

5. Conclusions

The effect of Cu on Ni in the catalytic transformation of glycerol is strongly governed by the geometrical effect. The most interesting feature of the present work is the marked difference in the effect of Cu on the catalytic activity of Ni for the glycerol conversion. In the case of the deep hydrogenolysis which produces CH_4 , the rupture of the C–C bond by hydrogenolysis decreases by addition of small amounts of Cu and continues to decrease until CH_4 be totally suppressed. As the Ni/Cu atomic ratio decreases the dehydration–dehydrogenation routes starts to prevail, and hydroxyacetone, pyruvaldehyde, lactic acid and pyruvaldehyde are formed. In addition, as revealed by our XPS results, when the Ni/Cu atomic ratio decreases a progressive enrichment of Cu in the catalyst surface occurs, decreasing the total number of exposed Ni atoms and suppressing totally the deep hydrogenolysis. FTIR of adsorption of CO indicated that the geometrical effect was dominant over the electronic effect. In this respect the bridge CO molecule bounded to metallic Ni was eliminated by the addition of Cu. In terms of selectivity, as a consequence of the decrease in the Ni/Cu atomic ratio the dehydration products prevail.

Acknowledgments

B.C. Miranda gratefully acknowledges the Universitat Rovira i Virgili (URV) and Universidad de Costa Rica (UCR) for the financial support. We also would like to acknowledge European Synchrotron Radiation Facility (ESRF) and Brazilian National Laboratory Light Synchrotron (LNLS) for the user facilities for XRD and XANES measurements, respectively. Thanks for Ministry of Science and Technology of Spain for the financial support for the Juan de la Cierva program (JCI-2010-07328). We also would like to acknowledge Dr. Germán Castro, Dr. Iván da Silva and Dr. Alvaro Muñoz for the technical support offered at the ESRF (experiment MA-1525). JS gratefully acknowledges the support of this work by the US Department of Energy (DOE), Office of Science, Office of Basic Energy Sciences, Chemical Sciences, Geosciences, and Biosciences Division. The research related to the FTIR of adsorption of CO (Proposal 48209) was performed in the Environmental Molecular Sciences Laboratory (EMSL), a national scientific user facility sponsored by the DOE Office of Biological and Environmental Research located at Pacific Northwest National Laboratory (PNNL). PNNL is operated for the US DOE by Battelle Memorial Institute under contract number DE-AC05-76RL01830.

References

- [1] L. Guo, J. Zhou, J. Mao, X. Guo, S. Zhang, *Appl. Catal., A: Gen.* 367 (2009) 93–98.
- [2] P. Werle, M. Morawietz, S. Lundmark, K. Sørensen, E. Karvinen, J. Lehtonen, in: *Wiley-VCH (Ed.), Ullmann's Encyclopedia of Industrial Chemistry*, Wiley-VCH, Weinheim, 2006.
- [3] R.D. Cortright, M. Sanchez-Castillo, J.A. Dumesic, *Appl. Catal., B: Environ.* 39 (2002) 353–359.
- [4] M. Pagliaro, R. Ciriminna, H. Kimura, M. Rossi, C. Della Pina, *Angew. Chem. Int. Ed.* 46 (2007) 4434–4440.
- [5] C.H. Zhou, J.N. Beltramini, Y.X. Fan, G.Q. Lu, *Chem. Soc. Rev.* 37 (2008) 527–549.
- [6] M.A. Dasari, P.P. Kiatsimkul, W.R. Sutterlin, G.J. Suppes, *Appl. Catal., A: Gen.* 281 (2005) 225–231.
- [7] C. Montassier, J.C. Ménéz, L.C. Hoang, C. Renaud, J. Barbier, *J. Mol. Catal.* 70 (1991) 99–110.
- [8] B. Katryniok, S. Paul, F. Dumeignil, *ACS Catal.* 3 (2013) 1819–1834.
- [9] S. Sato, M. Akiyama, R. Takahashi, T. Hara, K. Inui, M. Yokota, *Appl. Catal., A: Gen.* 347 (2008) 186–191.
- [10] L. Ma, D. He, Z. Li, *Catal. Commun.* 9 (2008) 2489–2495.
- [11] Y. Nakagawa, K. Tomishige, *Catal. Sci. Technol.* 1 (2011) 179–190.
- [12] J. ten Dam, U. Hanefeld, F. Kapteijn, K. Djanashvili, U. Hanefeld, *Catal. Commun.* 13 (2011) 1–5.
- [13] T. Kurosaka, H. Maruyama, I. Naribayashi, Y. Sasaki, *Catal. Commun.* 9 (2008) 1360–1363.
- [14] D. Roy, B. Subramaniam, R.V. Chaudhari, *Catal. Today* 156 (2010) 31–37.
- [15] T. Miyazawa, Y. Kusunoki, K. Kunimori, K. Tomishige, *J. Catal.* 240 (2006) 213–221.
- [16] J. Chaminand, L. Djakovitch, P. Gallezot, P. Marion, C. Pinel, C. Rosier, *Green Chem.* 6 (2004) 359–361.
- [17] A. Alhanash, E.F. Kozhevnikova, I.V. Kozhevnikov, *Catal. Lett.* 120 (2008) 307–311.
- [18] F. Auneau, C. Michel, F. Delbecq, C. Pinel, P. Sautet, *Chem. Eur. J.* 17 (2011) 14288–14299.
- [19] S. Xia, Z. Yuan, L. Wang, P. Chen, Z. Hou, *Appl. Catal., A: Gen.* 403 (2011) 173–182.
- [20] F. Auneau, S. Noël, G. Aubert, M. Besson, L. Djakovitch, C. Pinel, *Catal. Commun.* 16 (2011) 144–149.
- [21] I. Jiménez-Morales, F. Vila, R. Mariscal, A. Jiménez-López, *Appl. Catal., B: Environ.* 117–118 (2012) 253–259.
- [22] B.C. Miranda, R.J. Chimentão, J.B.O. Santos, F. Gispert-Guirado, J. Llorca, F. Medina, F. López Bonillo, J.E. Sueiras, *Appl. Catal., B: Environ.* 147 (2014) 464–480.
- [23] P. Li, J. Liu, N. Nag, P.A. Crozier, *J. Catal.* 262 (2009) 73–82.
- [24] F. Bonet, S. Grugeon, L. Dupont, R. Herrera Urbina, C. Guéry, J.M. Tarascon, *J. Solid State Chem.* 172 (2003) 111–115.
- [25] J.H. Sinfelt, *Bimetallic Catalysts: Discoveries, Concepts, and Applications*, John Wiley & Sons, Inc., United States of America, 1931.
- [26] I. Gandarias, J. Requies, P.L. Arias, U. Armbruster, A. Martin, *J. Catal.* 290 (2012) 79–89.
- [27] C.A. Bernardo, I. Alstrup, J.R. Rostrup-Nielsen, *J. Catal.* 96 (1985) 517–534.
- [28] D.G. Lahr, B.H. Shanks, *Ind. Eng. Chem. Res.* 42 (2003) 5467–5472.
- [29] J.R. Anderson, K.C. Pratt, *Introduction to Characterization and Testing of Catalysts*, Academic Press, New York, NY, 1985.
- [30] I. Chen, S. Lin, D. Shiue, *Ind. Eng. Chem. Res.* 27 (1988) 926–929.
- [31] I. Chen, D.W. Shiue, *Ind. Eng. Chem. Res.* 27 (1988) 429–434.
- [32] J.R.A. Sietsma, H. Friedrich, A. Broersma, M. Versluis-Helder, A. Jos van Dillen, P.E. de Jongh, K.P.d. Jong, *J. Catal.* 260 (2008) 227–235.
- [33] G. Li, L. Hu, J.M. Hill, *Appl. Catal., A: Gen.* 301 (2006) 16–24.
- [34] S. Velu, K. Suzuki, M. Vijayaraj, S. Barman, C.S. Gopinath, *Appl. Catal., B: Environ.* 55 (2005) 287–299.
- [35] K. Shimizu, K. Kon, K. Shimura, S.S.M.A. Hakim, *J. Catal.* 300 (2013) 242–250.
- [36] H. Kusaka, M. Onuki, Y. Hara, *Appl. Catal.* 185 (1999) 227–235.
- [37] M. Kang, M.W. Song, T.W. Kim, K.L. Kim, *Can. J. Chem. Eng.* 80 (2002) 63–70.
- [38] A.R. Naghash, T.H. Etsell, S. Xu, *Chem. Mater.* 18 (2006) 2480–2488.
- [39] A. Carrero, J.A. Calles, A.J. Vizcaíno, *Chem. Eng. J.* 163 (2010) 395–402.
- [40] Y. Li, J. Chen, L. Chang, Y. Qin, *J. Catal.* 178 (1998) 76–83.
- [41] M. Khzouza, J. Wood, B. Pollet, W. Bujalski, *Int. J. Hydrogen Energy* 38 (2013) 1664–1675.
- [42] J.-H. Lin, P. Biswas, V.V. Gulians, S. Misture, *Appl. Catal., A: Gen.* 387 (2010) 87–94.
- [43] J. Lif, I. Odenbrand, M. Skoglundh, *Appl. Catal., A: Gen.* 317 (2007) 62–69.
- [44] E.L. de León-Quiroz, B.A. Puente-Urbina, D. Vázquez-Obregón, L.A. García-Cerda, *Mater. Lett.* 91 (2013) 67–70.
- [45] F. Vila, M. López Granados, M. Ojeda, J.L.G. Fierro, R. Mariscal, *Catal. Today* 187 (2012) 122–128.
- [46] B.D. Cullity, S.R. Stock, *Elements of X-Ray Diffraction*, Addison-Wesley, United States of America, 2001.
- [47] A. Hornés, P. Bera, M. Fernández-García, A. Guerrero-Ruiz, A. Martínez-Arias, *Appl. Catal., B: Environ.* 111–112 (2012) 96–105.
- [48] J. Batista, A. Pintar, J.P. Gomilšek, A. Kodre, F. Bornette, *Appl. Catal., A: Gen.* 217 (2001) 55–68.
- [49] A. Kitla, O.V. Safonova, K. Föttinger, *Catal. Lett.* 143 (2013) 517–530.
- [50] K. Hadjiivanov, M. Mihaylov, D. Klissurski, P. Stefanov, N. Abadjieva, E. Vasileva, L. Mintchev, *J. Catal.* 185 (1999) 314–323.
- [51] J.W.C. Liberatori, R.U. Ribeiro, D. Zanchet, F.B. Noronha, J.M.C. Bueno, *Appl. Catal., A: Gen.* 327 (2007) 197–204.
- [52] X. Zhu, Y.-p. Zhang, C.-j. Liu, *Catal. Lett.* 118 (2007) 306–312.
- [53] M. Mihaylov, O. Lagunov, E. Ivanova, K. Hadjiivanov, *Top. Catal.* 54 (2011) 308–317.
- [54] N.-Y. Topsøe, H. Topsøe, *J. Mol. Catal. A: Chem.* 141 (1999) 95–105.
- [55] W. Suprun, M. Lutecki, T. Haber, H. Papp, *J. Mol. Catal. A: Chem.* 309 (2009) 71–78.
- [56] A. Corma, P.J. Miguel, A.V. Orchilles, *J. Catal.* 145 (1994) 171–180.
- [57] F.F. de Sousa, H.S.A. de Sousa, A.C. Oliveira, M.C. Junior, A.P. Ayala, E.B. Barros, B.C. Viana, J.M. Filho, A.C. Oliveira, *Int. J. Hydrogen Energy* 37 (2012) 3201–3212.
- [58] A.C. Ferrari, J. Robertson, *Phys. Rev. B: Condens. Matter* 61 (2000) 14095–14107.
- [59] A.C. Ferrari, B. Kleinsorge, G. Adamopoulos, J. Robertson, W.I. Milne, V. Stolojan, L.M. Brown, A. LiBassi, B.K. Tanner, *J. Non-Cryst. Solids* 266–269 (2000) 765–768.
- [60] J.H. Sinfelt, *Adv. Catal.* 23 (1973) 91.
- [61] P. Biloen, J.N. Helle, H. Verbeek, F.M. Dautzenberg, W.M.H. Sachtler, *J. Catal.* 63 (1980) 112.
- [62] Y. Soma-Noto, W.M.H. Sachtler, *J. Catal.* 32 (1974) 315.
- [63] L. Pauling, *Proc. R. Soc. London, Ser. A* 196 (1949) 243.
- [64] G. Bylholder, *J. Phys. Chem.* 68 (1964) 2772.